Check for updates

RESEARCH ARTICLE

NANO · MICRO small
www.small-journal.com

Structural Modifications due to Bi-Doping in $MAPbBr_3$ Single Crystals and Their Impact on Electronic Transport and Stability

*Sarah Su-O Youn, Gee Yeong Kim, and William Jo**

Doping strategy in lead halide perovskites is essential to enhance its optoelectrical properties and expand the potential applications. In this work, the mechanisms, for how dopants affect the overall structural, optical, electrical, and chemical properties and stability of lead halide perovskite materials, are investigated. This is done by specifically considering various bismuth (Bi) doping concentrations in $MAPbBr_3$ single crystals grown using the inverse temperature crystallization method. The resultant doped single crystals exhibit a saturation point when Bi concentration exceeds 0.063% which is considered an optimum doping point. The highest thermal stability is also achieved at this doping concentration among the doped single crystals. This study clearly identifies how Bi doping affects the properties of $MAPbBr_3$ and extends to consider stability, which has not been fully considered for MA-based perovskites previously. This will provide a clear understanding of evaluating doped perovskite materials for enhanced material properties, device performance, and stability.

1. Introduction

Organic-inorganic lead halide perovskites ($MAPbX_3$, X = Cl^-, Br^-, I^-) have been widely incorporated into various optoelectronic devices, including solar cells, LEDs, photodetectors, and X-ray detectors. Facile synthesis and low material costs ensure considerable opportunities for developing perovskite materials for further device commercialization. However, lead halide perovskites are intrinsically complex materials, where the presence of various types of interactions and structural disorders may significantly influence the material properties.[1] In this sense, perovskite single crystals are ideal targets to investigate material properties since they exhibit higher crystallinity and uniformity, lower trap density, superior optoelectrical properties, and enhanced stability compared to polycrystalline thin films.[2]

Doping can help improve the optical and electrical properties of semiconductor materials, with many traditional semiconductor materials benefiting from doping. For example, Si is a poor conductor that exhibits p or n-type conduction after impurity doping, commonly with boron (B) or phosphorus (P). Perovskite structure compositional tunability facilitates doping with several metal monovalent (acceptor)/divalent/trivalent (donor) cations, including Ag^+, Zn^{2+}, Mn^{2+}, Al^{3+}, Bi^{3+}, Yb^{3+}, and Ln^{3+}.[3] In particular, lead halide perovskite p or n-type conduction can be controlled by incorporating such dopants, and this doping strategy in perovskites is essential for them to enhance optoelectrical properties and expand potential applications into devices beyond just optoelectronics, a considerable step for industrial applications. However, many perovskite doping issues remain unresolved, such as optimal (and practical) dopant positioning in the crystal lattice, and how the metal ions regulate the material properties.

Bismuth (Bi) is the most frequently used dopant in lead halide perovskites due to its similar ionic radius to Pb. Abdelhady et al. (2016) reported doping $MAPbBr_3$ single crystals with variant trivalent metal ions (Bi^{3+}, In^{3+}, and Au^{3+}) in the perovskite precursor solution, establishing charge doping and band gap tuning possibilities for perovskite single crystals.[3d] Several subsequent studies have considered Bi doping, introducing Bi to stabilize the α-phase of $CsPbI_3$ and $FAPbI_3$ at room temperature,[4] enhancing stability and increasing perovskite conductivity due to the excess electron from Bi^{3+}. Thus, Bi has become a promising dopant for device development.

However, Bi also generates negative effects on perovskite optoelectronic properties. Several recent studies on Bi into $MAPbBr_3$ have shown that increased absorbance range does not cause bandgap narrowing, but is due to energy disorder and doping

S. S.-O Youn, W. Jo
Department of Physics
Ewha Womans University
Seoul 03760, Republic of Korea
E-mail: wmjo@ewha.ac.kr
G. Y. Kim
Advanced Photovoltaic Research Center
Korea Institute of Science and Technology
Seoul 02456, Republic of Korea

The ORCID identification number(s) for the author(s) of this article can be found under https://doi.org/10.1002/smll.202407141

© 2024 The Author(s). Small published by Wiley-VCH GmbH. This is an open access article under the terms of the Creative Commons Attribution-NonCommercial-NoDerivs License, which permits use and distribution in any medium, provided the original work is properly cited, the use is non-commercial and no modifications or adaptations are made.

DOI: 10.1002/smll.202407141

does not affect the bandgap.[5] Doping Bi into perovskite structure introduces traps that act as material defects, facilitating recombination centers.[5a–c,e] Photovoltaic devices fabricated using Bi-doped perovskite have also exhibited diminished device parameters due to generated defect states.[6] Although Bi acts as a defect in single crystals and hence is not generally suitable for optoelectronics, these Bi-doped crystals have become relatively commonly employed for photodetectors and photodiodes since 2020 which has been reported to show enhanced photo responsivity and detectivity.[7] This is because p-n perovskite homojunctions have small lattice mismatches, continuous band alignment, and smaller carrier trap sites.[7a,d,8] Trading-off between positive and negative doping effects requires specific evaluation. Hence, Bi doping impact in lead halide perovskites requires further study.

This work investigates the effects of doping Bi into single crystal $MAPbBr_3$ by controlling the dopant concentration in the precursor solution. Although there have been several reports investigating the Bi doping effect in lead halide perovskite, a clear evaluation of how doping concentration affects the structural, optical, electrical, and chemical properties have not been fully exploited. We note that a trade-off between defect formation and electrical transport, stability exists, as will be discussed. X-ray diffraction (XRD) and Raman spectroscopy investigation help to understand how Bi doping affects and incorporates into the perovskite crystal structure. Resultant optical and electrical properties confirm that doped single crystals do not significantly differ from previously reported outcomes while suggesting an optimal doping concentration with a few trade-offs that will be discussed. Ultraviolet Photoelectron Spectroscopy (UPS) and Hall effect measurement confirmed n-doping, and strengthened chemical bonding due to Bi was identified with X-ray photoelectron spectroscopy (XPS), consistent with Raman results. Thermogravimetric analysis (TGA) and differential scanning calorimetry (DSC) support the evidence of an optimum doping concentration, where the doped sample achieves the highest thermal stability due to stronger chemical bonding and fewer defects generated in the crystal. Thus, this study confirms optimal doping concentrations can be defined to provide the best material properties, which should be considered for further applications using doped lead halide perovskite.

2. Results

2.1. Bi Substituting for Pb in Single Crystals

Bi-doped $MAPbBr_3$ single crystals were grown using the inverse temperature crystallization (ITC) method as previously reported.[9] However, rather than mixing two separate solutions ($MABr+PbBr_2$ and $MABr+BiBr_3$,[3d,10] or $MABr+PbBr_2$ and pure $BiBr_3$[5c,11]) for the final precursor solution preparation step, we added the appropriate amount of $BiBr_3$ in the precursor solution immediately,[5a,b,d] ensuring nominal Bi concentration in the solution = 1%, 2%, 5%, 10%, or 15%. Han et al. showed the Bi content that can be substituted in the crystal is maintained to a fixed amount when more than 20% of Bi is added to the solution,[5d] i.e., Bi incorporation in the crystal is limited by some as yet unexplained mechanism. We have previously grown crystals from a feed solution containing 20% Bi, but crystal nucleation was randomly generated at higher temperatures compared to the lower concentrations. Hence, 15% Bi in the solution was chosen for the highest doped crystal precursor.

Figure 1a shows the typical ITC growth process, with Figure 1b presenting the heating process for crystallization. The heating speed was reduced as temperature increased to eliminate unnecessary crystal nucleation and encourage a few number of large and uniform single crystal growths. Undoped and lightly doped single crystals with Bi concentrations of 0%, 1%, 2%, and 5% in the solution typically appeared at temperatures ≈90–100 °C. In contrast, solutions containing higher Bi concentrations of 10% and 15% were observed at elevated temperatures above 110 °C. Figure 1c shows typically grown Bi-doped $MAPbBr_3$ single crystals with dark purplish colors from increasing Bi in the precursor solution. These samples were labeled as Bi and Bi+Pb ratio in the crystal which were 0%, 0.019%, 0.042%, 0.063%, 0.11%, and 0.19%, obtained through inductively coupled plasma–optical emission spectroscopy (ICP-OES) (Figure S1, Supporting Information). Although Bi content in single crystals was significantly less than Bi concentration in the precursor solution, the Bi content increased linearly, indicating successful Bi substitution into the crystals.

Scanning electron microscopy and energy dispersive spectroscopy (SEM-EDS) on the freshly cleaved single crystals were used to examine Bi distribution throughout the crystals, i.e., relatively evenly distributed throughout the crystal or tending to preferentially occur near the surface. First, the middle part of each crystal was scanned, far away from the crystal's edges or surface. Figure S2 (Supporting Information) shows the crystal's cleaved surface and corresponding EDS analysis for Br, Pb, Bi, C, and N. SEM images exhibit clean grain boundary-free surfaces of the single crystals. EDS confirmed Bi was uniformly incorporated within the single crystals.

Next, SEM-EDS line scans were employed to analyze the distribution of Bi near the surface of cleaved single crystals. **Figure 2** presents the SEM images of cleaved single crystals and their corresponding EDS line scan profiles for Br, Pb, Bi, and C. The surface of the single crystal is delineated with a dotted line in the SEM image. The EDS line scan was initiated from the exterior of the single crystal surface and progressed toward the bulk region. A pronounced carbon signal is observed at the surface region of the single crystals, attributed to exposure to air. This carbon signal diminished as the scan proceeded into the bulk region of the single crystal. In comparison to other samples, Figure 2c,d displays Br, Pb, and Bi signals from the initial scan point, indicating the detection of the bare surface of the single crystals. This observation is corroborated by the SEM images, which show an absence of a distinct boundary between air and the single crystal for these samples, unlike the others. Overall, the doped samples exhibit consistent and continuous Bi signals within the single crystal region, providing evidence of uniform Bi distribution throughout the crystal.

Figure 3 shows grown crystal structural qualities and properties, determined from XRD and rocking curves. XRD results for the single crystals (Figure 3a) present characteristic peaks for (001), (002), and (003) at 14.96°, 30.14°, and 45.89°, respectively, from the pristine single crystal. Some slight peak shifting to a larger degree was also exhibited, indicating lattice contraction,

© 2024 The Author(s). Small published by Wiley-VCH GmbH

16136829, 2024, 51, Downloaded from https://onlinelibrary.wiley.com/doi/10.1002/smll.202407141 by Ewha Womans University Library, Wiley Online Library on [16/01/2025]. See the Terms and Conditions (https://onlinelibrary.wiley.com/terms-and-conditions) on Wiley Online Library for rules of use; OA articles are governed by the applicable Creative Commons License

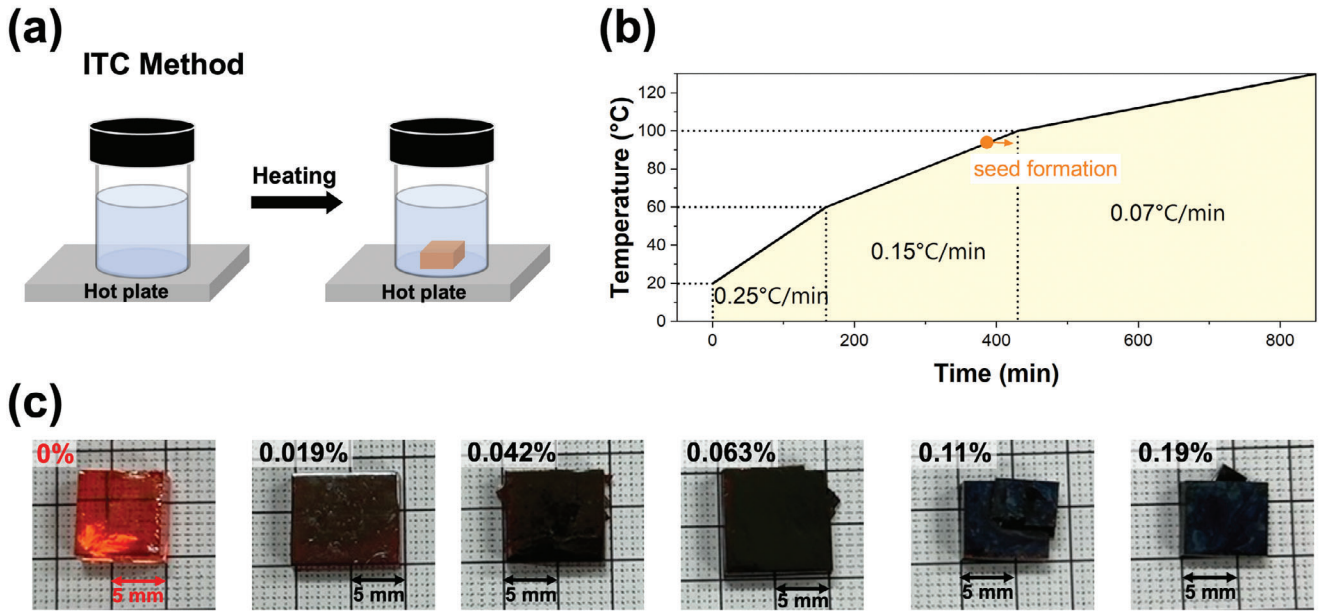


Figure 1. a) Schematic illustration of the single crystal nucleation method. b) Heating rate used for the crystallization process. c) Doped and undoped $MAPbBr_3$ single crystals.

although the peak shift is quite subtle. This tells us that Bi doping does not affect crystal growth or alter the perovskite crystal structure. Figure 3b shows X-ray rocking curve analysis for the first major XRD peaks using full width at half maximum (FWHM) to compare crystal quality; FWHM = 0.045°, 0.039°, 0.042°, 0.049°, 0.057°, and 0.067° for 0%, 0.019%, 0.042%, 0.063%, 0.11%, and 0.19% doped single crystals, respectively. This monotonically increasing FWHM indicates continuous bismuth incorporation into the crystal leads to disorder in the crystal, similar to previous studies.[10]

All XRD patterns for crushed powdered single crystals exhibited sharp peaks (Figure 3c), with no new or diminished peaks appearing after doping. This observation indicates that Bi doping does not deteriorate the perovskite crystal structure, consistent with both single-crystal samples and previous reports.[5b,c,6,10–11] This is further supported by the Goldschmidt tolerance factor (t),[12] which was calculated to be 0.84 and does not exhibit a significant difference after adding the ionic radius value for Bi. Rietveld refinement was performed on the powder XRD patterns using Fullprof software (see Figure S3, Supporting Information).[13] The refinement results verified that the synthesized single crystals all adopt the cubic perovskite structure, with space group *Pm-3m*. Figure 3d shows the fitted lattice parameters of the undoped sample, with a = 5.931 Å, which is reduced to a = 5.928 Å for the highest doped sample. This lattice contraction is likely due to the different radius size between Bi^{3+} (1.03 Å) and Pb^{2+} (1.19 Å).[14] The unit cell volume contraction follows the same trend of the lattice parameter. Pb—Br bond length and $PbBr_6^{4-}$ octahedra volume change is plotted in Figure 3e, which may also be attributed to the lattice parameter reduction. Jedlicka et al. proposed that Bi substituting Pb, along with donating an excess electron, results in compressive chemical strains and a decrease in lattice constant,[11] which supports our results. Figure 3f illustrates the $PbBr_6^{4-}$ octahedra schematic figure of 0% and 0.063% doped samples using VESTA software. As illustrated, Bi occupancy at the B site increases after doping, substituting Pb, based on the refinement results. However, it is important to note that Figure 3f is not an exact depiction of the $PbBr_6^{4-}$ octahedral structure of the doped $MAPbBr_3$ crystal but rather a schematic illustration to present that Bi substitutes Pb.

Figure 4 shows Raman scattering spectroscopy results performed to investigate the vibrational phonon modes for the single crystals and further explore structural features. Raman spectra for the single crystals occur in distinct regions: 50–250 and 250–3500 cm^{-1} with assigned peaks summarized in **Table 1**. Overall spectra for all samples confirmed the $MAPbBr_3$ cubic structure[9,15] which is consistent with XRD results. Figure 4a shows low-frequency vibration modes at 50–250 cm^{-1} belonging to the $PbBr_6^{4-}$ octahedra frame,[16] whereas high-frequency modes at 250–3500 cm^{-1} (Figure 4b) are assigned to MA^+ cation's vibrational modes which are highly sensitive to the microenvironment and chemical interactions between the organic cation and the inorganic framework mainly taking place at the NH_3 end of MA^+.[5d,17] This outcome confirms Raman spectroscopy as an essential tool for understanding how Bi doping affects the vibration modes to identify its impact on the crystal structure. Overall peak intensities achieved the highest intensity for the 0.019% sample and gradually decreased with increasing Bi content. Thus, although a small amount of Bi doping enhances crystal quality,[5d,9,18] additional incorporation leads to crystal disorder, which is supported by the XRD rocking curve result.

We took a detailed look into the low-frequency vibration mode in Figure 4a. The peaks of vibration mode ν_1 and ν_2 indicate the bending and stretching of the Pb—Br bond in the $PbBr_6^{4-}$ octahedra frame. While the ν_1 mode-assigned peak did not show significant peak shifting, the ν_2 mode-assigned peak shifted to higher wavenumber as doping concentration increased. The vibration mode is illustrated in Figure 4c and detailed ν_2 mode peak

© 2024 The Author(s). Small published by Wiley-VCH GmbH

16136829, 2024, 51, Downloaded from https://onlinelibrary.wiley.com/doi/10.1002/smll.202407141 by Ewha Womans University Library, Wiley Online Library on [16/01/2025]. See the Terms and Conditions (https://onlinelibrary.wiley.com/terms-and-conditions) on Wiley Online Library for rules of use; OA articles are governed by the applicable Creative Commons License

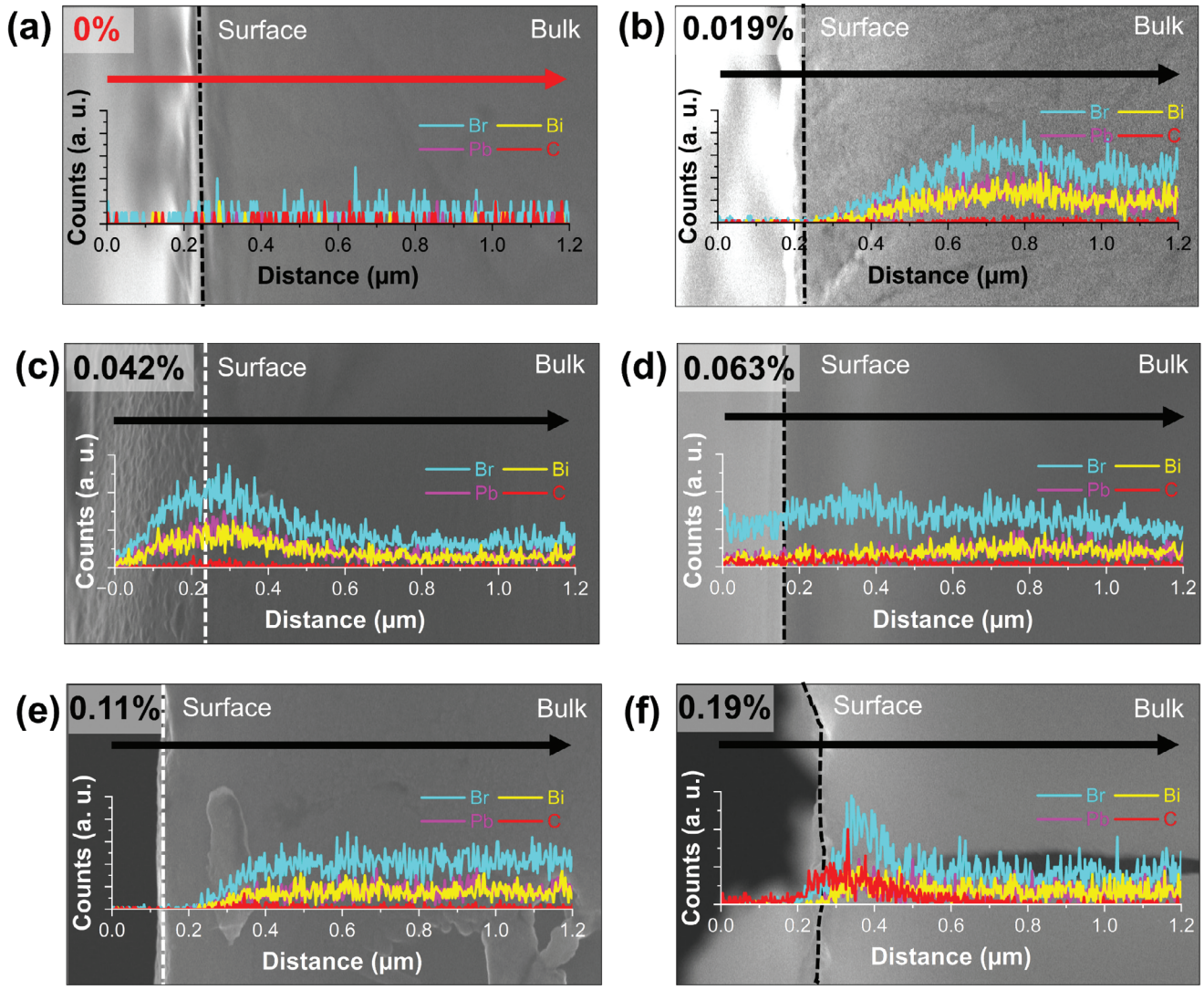


Figure 2. Cross-sectional SEM images and EDS line scan profile of Br, Pb, Bi, and C elements for a) 0%; b) 0.019%; c) 0.042%; d) 0.063%; e) 0.11%; and f) 0.19% Bi-doped $MAPbBr_3$ single crystals. (Line scan length: 1.2 μm, arrow indicates scan direction).

position and intensity are plotted as a function of Bi concentration in Figure 4d. Raman blue shift is known to indicate lattice contraction[19] due to Pb—Br bond length compression[20] as a result of Bi incorporation. The shorter Bi—Br bond length (2.87 Å)[21] compared with the Pb—Br bond length (2.97 Å)[22] probably leads to lattice contraction which is consistent with XRD. A similar trend in the ν_2 mode shift has been seen in a report by Li et al. where a pressure experiment was conducted on $MAPbBr_3$ and observed a similar peak shift trend in the low-frequency Raman range (100–200 cm^{-1}).[16b] Hence, the ν_2 mode blue shift supports evidence of Bi substituting for Pb with resulting lattice contraction. Han et al. reported that a Raman peak at 167 cm^{-1} relative to the $Bi_2Br_9^{3-}$ anion's stretching region in $MA_3Bi_2Br_9$ that appeared when Bi^{3+} accumulates on the surface of doped $MAPbBr_3$.[23] However, we were unable to identify any peaks at that position, i.e., no excess Bi appears to be present at the surface of the single crystals. The high-frequency vibration modes in Figure 4b show no significant peak shifting after doping. This means that Pb—Br bond compression does not seem to affect MA vibration modes and any phase transition behaviors which is consistent with the XRD results.

2.2. Optimum Doping Concentration

2.2.1. Photophysical Measurements Regarding Defect Formation

To further understand the photophysical properties of doped single crystals, UV–vis absorption was conducted. The absorbance offset in Figure S4 (Supporting Information) redshifted from 580 to 690 nm after doping, consistent with the darker colors of the doped single crystals. However, large single-crystal thickness often causes the optical bandgap to be overestimated when measured using UV–vis spectroscopy.[28] In addition, the absorbance spectra red shift due to a longer absorbance tail was generated as a result of deep trap states formed by defects inside the crystal,

© 2024 The Author(s). Small published by Wiley-VCH GmbH

16136829, 2024, 51, Downloaded from https://onlinelibrary.wiley.com/doi/10.1002/smll.202407141 by Ewha Womans University Library, Wiley Online Library on [16/01/2025]. See the Terms and Conditions (https://onlinelibrary.wiley.com/terms-and-conditions) on Wiley Online Library for rules of use; OA articles are governed by the applicable Creative Commons License

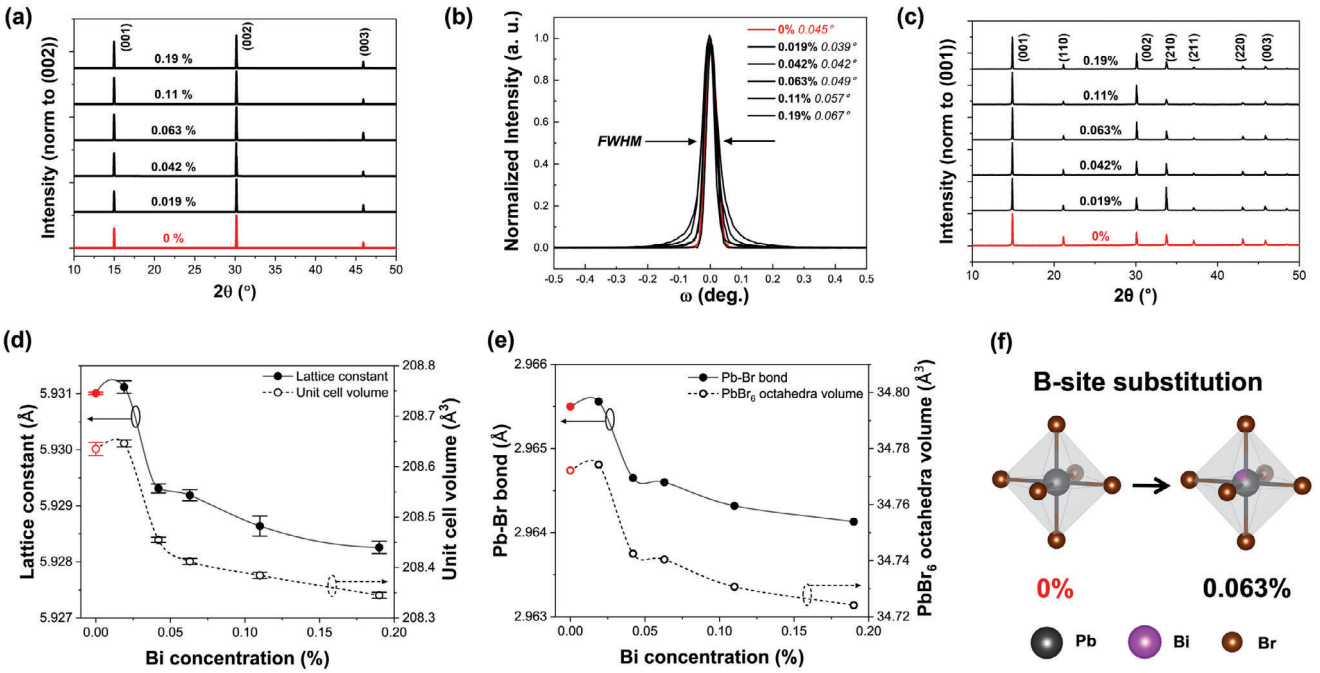


Figure 3. a) XRD patterns for pristine and Bi-doped $MAPbBr_3$ single crystals; b) Rocking curves from the first diffraction peaks; c) XRD patterns for crushed single crystals powders; $MAPbBr_3$ d) lattice constant and unit cell volume; e) Pb—Br bond length and $PbBr_6$ octahedron volume; f) Illustration of the $PbBr_6$ octahedra for 0% and 0.063% doped samples determined through Rietveld refinement from powder XRD.

and not an actual band gap shift for the doped crystals.[5b,29] We estimated the Urbach energy (E_U) from Figure S4 (Supporting Information) using the following equation:

$$E_U = \frac{E - E_g}{\ln\left(\frac{\alpha(E)}{\alpha_g}\right)} \quad (1)$$

where E_g, $\alpha(E)$, and α_g are the band gap energy, absorption coefficient spectra, and α value at $E = E_g$.[30]

Figure S5 (Supporting Information) shows $\ln(\alpha)$ with respect to E, used to calculate E_U with resultant values summarized in **Figure 5a**. E_U ≈20 and 60 meV for the undoped and doped samples, respectively, are consistent with previous reports.[5a,b] Thus, E_U increases significantly after Bi doping, leading to a longer Urbach tail that makes the optical absorbance seem to shift to a longer wavelength. The increase in E_U demonstrates lattice distortion and energetic disorder in the crystal due to defects formed in the crystal.[31]

We used photoluminescence (PL) measurement to observe the band gap and photoexcited charge carrier transport properties. The PL absorption peak presented in Figure S6 (Supporting Information) is unchanged, suggesting a fixed band gap at 2.28 eV for the undoped and doped single crystals. This is consistent with previous reports that have shown the band gap does not change through PL and ellipsometry measurements.[5a,b] PL quenching after Bi doping (see Figure S6a, Supporting Information) confirms that doping generated defect formation in $MAPbBr_3$ subsequently generating carrier trapping, consistent with increased Urbach tail from UV–vis spectroscopy. This effect was also exhibited in Bi-doped $MAPbBr_3$ thin films.[5e] The trivalent Bi^{3+} can act as a deep electron trap when substituting divalent Pb^{2+}.[32] Thus, Bi incorporation acts as a defect in $MAPbBr_3$, consistent with previous reports.[5a,c,e,6] The PL peak of pristine $MAPbBr_3$ contains an additional peak at ≈576 nm, with the main peak at 546 nm. This additional peak is known to be generated from the photon recycling effect caused by re-emission after self-absorption and internal reflections in the thick crystal.[33] The additional peak does not appear in the Bi-doped samples which suggests that photon recycling is suppressed after doping.[5a]

Identifying the change in PL FWHM is important as it contains crucial information on defect states in the material. The PL peaks of all samples have been normalized to compare the FWHM (see Figure S6b, Supporting Information). A large difference between the undoped and doped samples can be sighted, with the values plotted in Figure 5b. FWHM increases with increasing Bi concentration, due to increased defect states or shallow traps.[34] This is consistent with the PL quenching effect and Urbach energy increase. Figure 5a,b summarizing E_U, PL FWHM, and PL intensity follow similar trends with increasing Bi concentration, overall indicating that Bi doping promotes defect formation. Interestingly, the doped single crystal shows minimal defect at 0.063% Bi concentration, suggesting the existence of an optimum Bi doping concentration in $MAPbBr_3$ where the best optical properties will exist among the doped single crystals.

We categorized the doped samples into two regions: the "low doping region" (green background – 0.019%, 0.042%, and 0.063%) and the "high doping region" (orange background – 0.11% and 0.19%). This classification is based on experimental results which will be discussed in detail later and is used for convenience of comparison. We hypothesize that there exists an optimal doping concentration at which Bi incorporation into the

© 2024 The Author(s). Small published by Wiley-VCH GmbH

16136829, 2024, 51, Downloaded from https://onlinelibrary.wiley.com/doi/10.1002/smll.202407141 by Ewha Womans University Library, Wiley Online Library on [16/01/2025]. See the Terms and Conditions (https://onlinelibrary.wiley.com/terms-and-conditions) on Wiley Online Library for rules of use; OA articles are governed by the applicable Creative Commons License

perovskite lattice stabilizes, reaching a point of maximum effectiveness before causing distortion beyond this region. In other words, the distinction between low and high doping regions is based on whether the doped samples exhibit an inflection point in their properties, indicating an optimum doping concentration for achieving the best material characteristics among the doped samples. This will be further explored in the following sections.

2.2.2. Trade-Off in Electrical Properties

Space-charge limited current (SCLC) model was adopted to extract the trap density of the single crystals.[35] The device structure used for the measurement was a hole-only device with Au electrodes deposited on each side of the single crystal (see inset of Figure 5c). The measured *I–V* curves were divided into three regions: ohmic (red), trap-filling region (blue), and Child (purple) regions (Figure 5c–e).[36] Trap density (n_t) was determined from the trap-filled limit voltage, V_{TFL}, i.e., the voltage at which the current begins to increase rapidly, using the following equation,[37]

$$n_t = \frac{2V_{TFL}\varepsilon_r\varepsilon_0}{eL^2} \tag{2}$$

where ε_0 is the vacuum permittivity, ε_r is the relative dielectric constant ($\varepsilon_r = 25.5$),[9] e is the elementary charge (1.6×10^{-19} C), and L is the single crystal thickness.

The increase in trap density (Figure 5f) after Bi incorporation supports the photophysical measurements from Section 2.2.1 which indicate the generation of defects in $MAPbBr_3$. The rise in trap density negatively impacts device performance, particularly in solar cells, as traps facilitate electron-hole recombination, thereby reducing device efficiency. However, it is early to assert that Bi doping in $MAPbBr_3$ has exclusively negative effects.

The SCLC method is a two-probe vertical measurement, raising concerns about the accuracy of the measured values (especially conductivity due to contact resistance issues). Hence, we conducted Hall effect measurements using the Van der Pauw method to evaluate the electrical properties of the single crystals. A photograph of the Hall measurement device is shown in Figure S7 (Supporting Information). The resistivity of the undoped $MAPbBr_3$ single crystal was higher than the measurable range of the instrument. Therefore, mobility, conductivity, and carrier concentration values of the undoped samples were extracted from the SCLC measurement shown in Figure 5c.

The carrier mobility of the undoped single crystal was extracted by fitting the Mott-Gurney law,

$$J_d = \frac{9\varepsilon_r\varepsilon_0\mu V^2}{8L^3} \tag{3}$$

where J_d is the dark current density, μ is the mobility, and V is the voltage. Conductivity for the Ohmic region, σ, and carrier concentration, n_c, was calculated as,

$$n_c = \frac{\sigma}{e\mu} \tag{4}$$

These extracted values were used to identify trends among the doping concentration, serving for comparison only.

The conductivity, mobility, and carrier concentration of the doped single crystals obtained with the Van der Pauw method are plotted in Figure 5f,g together with the values of the undoped single crystal obtained through SCLC. The parameter values increased with higher Bi concentrations, indicating partial improvement in the electrical properties, which aligns with previous studies.[3d,5c,10] The result suggests that Bi donates an excess electron to the crystal lattice, enhancing conductivity, mobility, and carrier concentration and effectively n-doping the material. In addition, the Hall coefficient values, summarized in Table S1 (Supporting Information), confirm that the doped single crystals are all n-type. Given that $MAPbBr_3$ is typically a p-type intrinsic material, this n-doping effect of Bi is consistent with expectations.

Overall, the saturation of trap density, mobility, and conductivity all observed in the "high doping region" after reaching a peak value at 0.063% Bi concentration, indicates a potential limitation in doping concentration. We hypothesize that Bi successfully substitutes Pb up to a certain limit, beyond which an excessive Bi concentration fails to stably substitute Pb, leading to saturation and eventual deterioration of material properties. The underlying physical mechanisms that occur when Bi surpasses the optimum concentration require further investigation.

2.3. Chemical Properties Confirm Optimum Doping Concentration

2.3.1. Surface Chemical Interactions

To further substantiate the evidence of n-doping, we measured the work function and valence band using UPS. The shift observed in the secondary cut-off (SECO) region (Figure S8a, Supporting Information) reflects a change in work function upon doping with Bi. The work functions were calculated by subtracting the He I photon energy (21.22 eV) from the SECO offset energy. The difference between the Fermi energy (E_F) and valence band maximum (VBM) (Figure S8b, Supporting Information) was determined by applying a Gaussian fit to the valence band onset on a logarithmic scale. Using the band gap value of 2.28 eV, obtained from our PL results, we calculated the conduction band minimum (CBM) position and constructed the energy band diagram for all the single crystals, as shown in **Figure 6a**. Our findings indicate that the undoped $MAPbBr_3$ single crystal is an n-type intrinsic material. With the incorporation of Bi, the material transitions from a nearly intrinsic state to a highly n-doped semiconductor. This transition is consistent with the Hall measurements, which confirmed that the doped single crystals are all n-type semiconductors with enhanced conductivity.

Furthermore, we observed a gradual shift in electron affinity (EA) and ionization energy (IE) as the doping concentration increased. Here, as well as other measurement results illustrate the EA and IE value hitting a peak value at 0.063% Bi doping concentration (Figure S9, Supporting Information). Above 0.063% Bi doping, EA and IE do not exhibit a significant difference, which seems to show a saturation behavior. Doping usually has minimal impact on EA and IE, as it primarily shifts the E_F with little effect on the band structure.[38] The change in IE may be attributed

© 2024 The Author(s). Small published by Wiley-VCH GmbH

16136829, 2024, 51, Downloaded from https://onlinelibrary.wiley.com/doi/10.1002/smll.202407141 by Ewha Womans University Library, Wiley Online Library on [16/01/2025]. See the Terms and Conditions (https://onlinelibrary.wiley.com/terms-and-conditions) on Wiley Online Library for rules of use; OA articles are governed by the applicable Creative Commons License

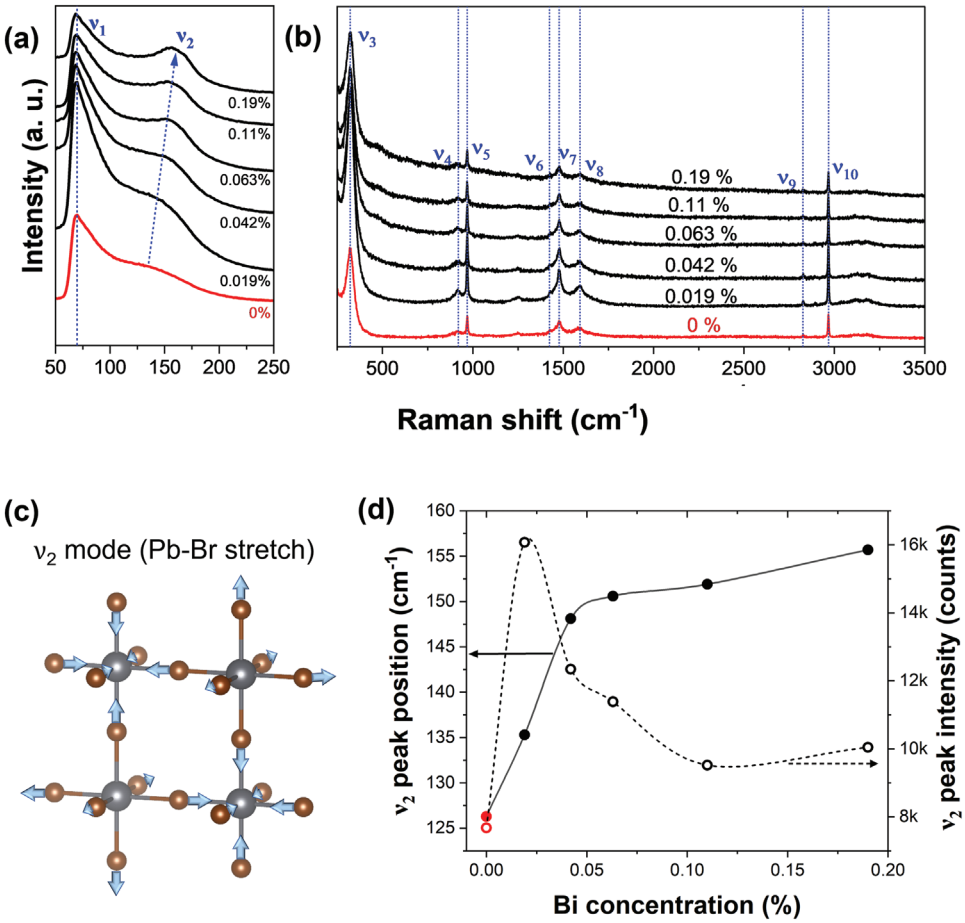


Figure 4. Raman spectra for pristine and Bi-doped $MAPbBr_3$ single crystals along the scanning range for a) 50–250 cm^{-1} and b) 250–3500 cm^{-1}. c) Illustration of the vibration for the ν_2 mode (Pb—Br stretching motion) and d) peak position and intensity of mode ν_2 plotted as a function of Bi doping concentration.

to a change in the chemical composition of the perovskite.[39] In this case, it appears that Bi doping not only introduces doping into $MAPbBr_3$ but also impacts surface chemistry. This phenomenon was likely detected with UPS, given the surface sensitivity of this measurement technique.

Table 1. Raman vibration modes and their mode assignments of pristine $MAPbBr_3$ single crystal from literature.

Mode	Position [cm^{-1}]	Assignment[a)]	Refs.
ν_1	70	δ_s (Br—Pb—Br)	[16]
ν_2	126	ν_{as} or ν_s (Pb—Br)	[16,24]
ν_3	322	τ (MA)	[16a,25]
ν_4	915	ρ (MA)	[16a,17,26]
ν_5	969	ν (C—N)	[16a,17,25–26]
ν_6	1428	δ_s (CH_3)	[16a,25b]
ν_7	1480	δ_{as} (NH_3^+)	[16a,25b,26]
ν_8	1592	δ_{as} (NH_3^+)	[16a,25b]
ν_9	2827	ν_{as} (C—H)	[25b,27]
ν_{10}	2967	ν_{as} (CH_3)	[16a,17]

[a)] ν: stretching, δ: bending, ρ: rocking, τ: torsion, s: symmetric, as: asymmetric

The surface chemical interaction and Bi ion doping were further confirmed through XPS. Figure S10a (Supporting Information) shows XPS survey scans that exhibit new Bi peaks that are present only in the doped single crystals, confirming the incorporation of Bi in all doped samples. This was also exhibited from the Bi 4f peaks from the narrow scan spectra (see Figure 6b). The C 1s peaks were calibrated to 284.8 eV for further investigation. XPS narrow scan spectra for the doped single crystals show that all C 1s, N 1s, Br 3d, and Pb 4f peaks shifted to higher binding energy after Bi doping (see Figure S10b–d, Supporting Information; Figure 6c). This shift indicates a modified chemical environment for $PbBr_6^{4-}$ octahedra and stronger Pb—Br interactions in the doped single crystals, consistent with previous reports.[3a,f]

The $PbBr_6^{4-}$ octahedral distortion is accompanied by changes in the lattice constant, as confirmed by XRD and Raman outcomes. Lattice contraction shortens the Pb—Br bonds and strengthens their interaction.[3f] A slight shift to lower binding energy occurs for C 1s, N 1s, Pb 4f, Br 3d, and Bi 4f peaks for the 0.11% and 0.19% samples. This suggests the existence of a specific optimal doping level (0.063% as discussed earlier), beyond which the dopant tends to segregate when doping content exceeds this level,[40] which we have identified as the high doping

© 2024 The Author(s). Small published by Wiley-VCH GmbH

16136829, 2024, 51, Downloaded from https://onlinelibrary.wiley.com/doi/10.1002/smll.202407141 by Ewha Womans University Library, Wiley Online Library on [16/01/2025]. See the Terms and Conditions (https://onlinelibrary.wiley.com/terms-and-conditions) on Wiley Online Library for rules of use; OA articles are governed by the applicable Creative Commons License

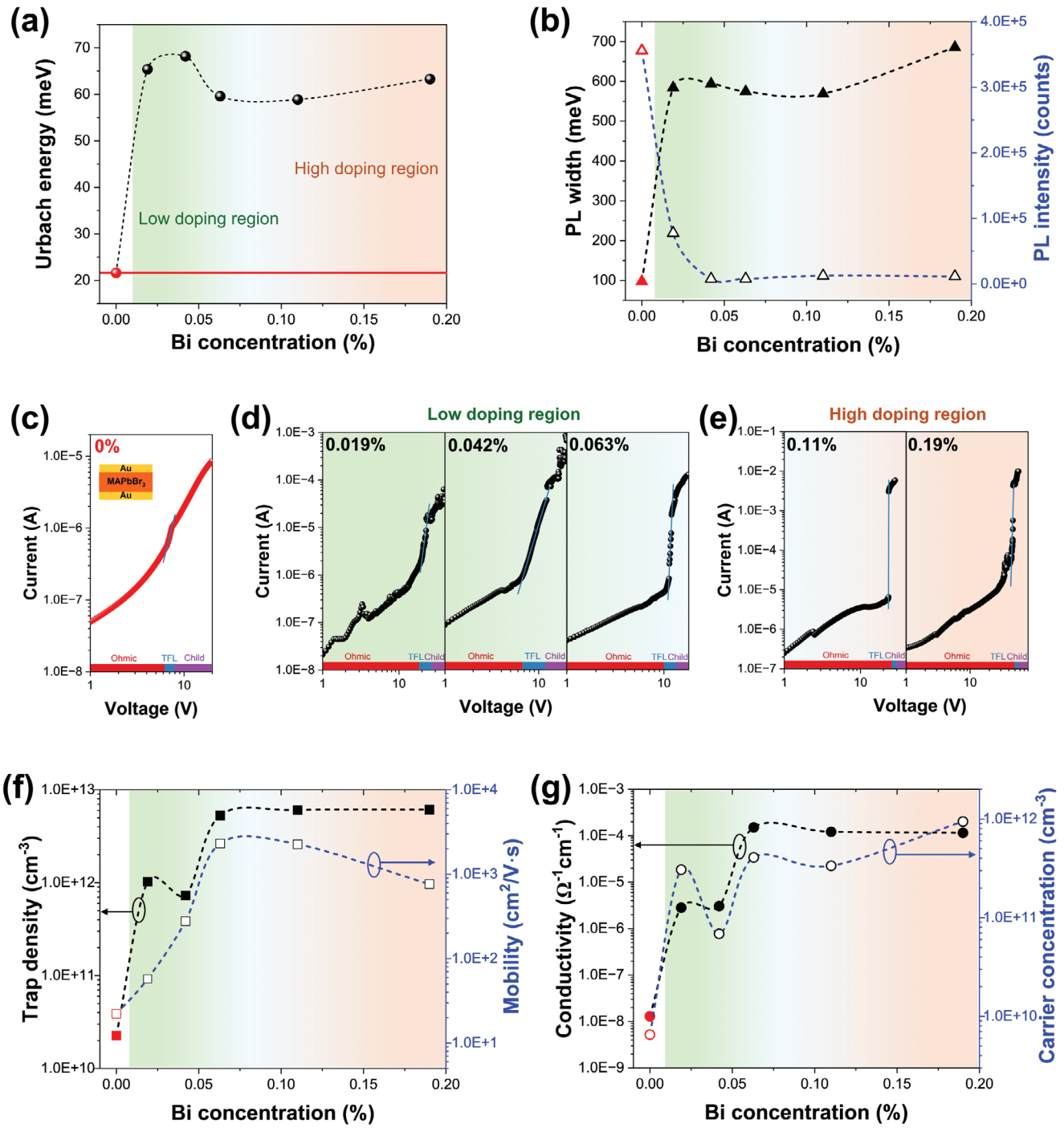


Figure 5. a) Urbach energy; b) PL FWHM and PL intensity for Bi-doped $MAPbBr_3$ single crystals; SCLC current–voltage curves of c) 0%, d) 0.019%, 0.042%, 0.063%, e) 0.11%, 0.19% doped single crystals; f) trap density and mobility; g) conductivity and carrier concentration of undoped and doped $MAPbBr_3$ single crystals obtained through SCLC and Hall measurement.

region. This change aligns with the trends observed in IE and EA as well.

Figure 6b displays the Bi 4f core level spectra. Intensity for the two Bi peaks increases with the Bi concentration in the single crystals, which is consistent with the rising Bi content. The peaks corresponding to Bi $4f_{5/2}$ and Bi $4f_{7/2}$ are attributed to Bi^{3+}, while the two smaller peaks are associated with metallic Bi (Bi^0).[10,41] The Pb 4f core level spectra, shown in Figure 6c, reveal metallic Pb (Pb^0) peaks at 140.9 and 136.1 eV. This formation of Pb^0 occurs when $MAPbBr_3$ is exposed to X-rays,[42] causing a chemical reaction with oxygen that leads to degradation.[43] This reaction was mirrored for $MAPbI_3$ as well.[44] Pb^0 acts as a deep

© 2024 The Author(s). Small published by Wiley-VCH GmbH

16136829, 2024, 51, Downloaded from https://onlinelibrary.wiley.com/doi/10.1002/smll.202407141 by Ewha Womans University Library, Wiley Online Library on [16/01/2025]. See the Terms and Conditions (https://onlinelibrary.wiley.com/terms-and-conditions) on Wiley Online Library for rules of use; OA articles are governed by the applicable Creative Commons License

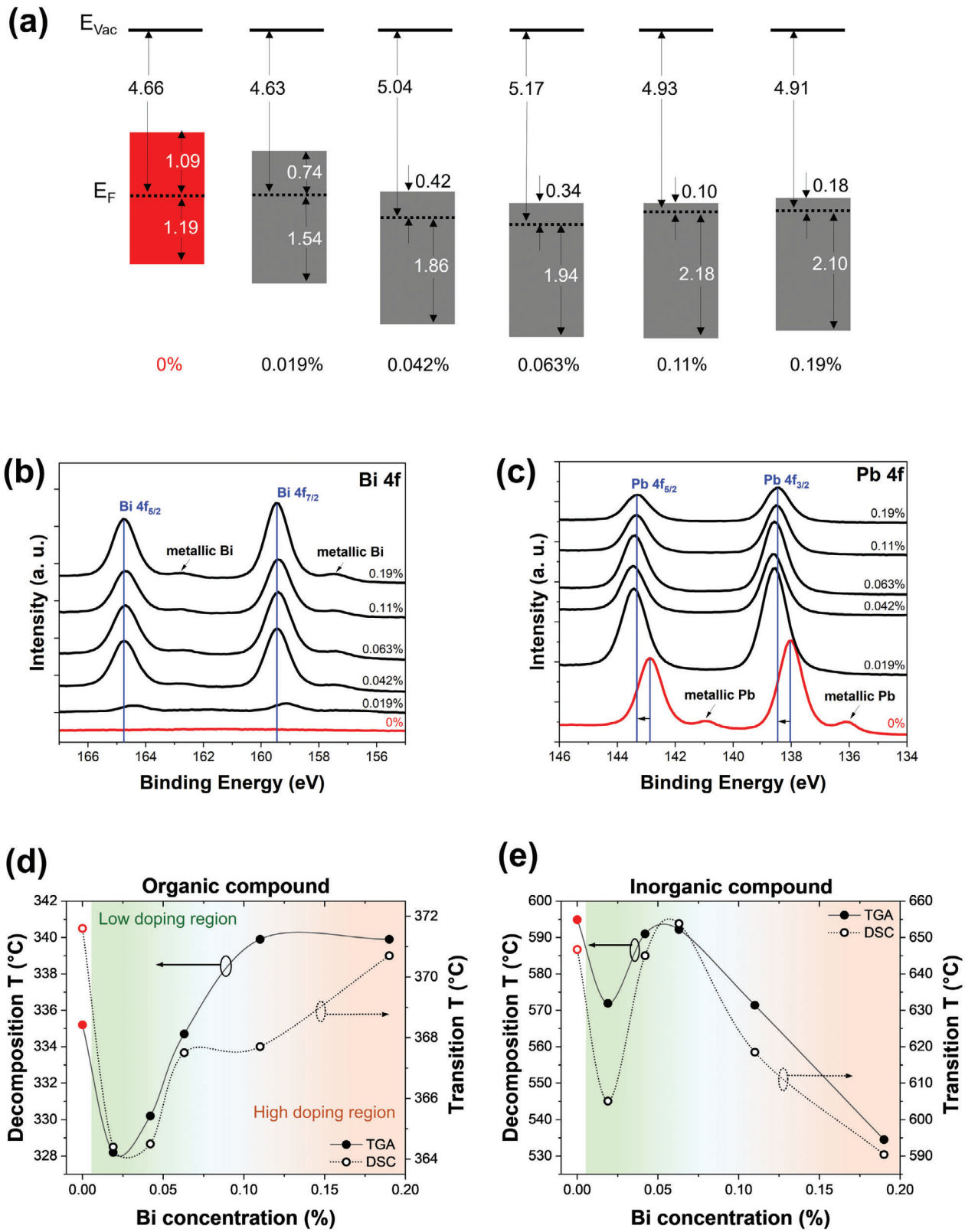


Figure 6. a) Energy levels of the single crystals derived from UPS spectra. XPS narrow scan spectra for b) Bi 4f, and c) Pb 4f in $MAPbBr_3$ single crystals with various Bi doping concentrations. Decomposition temperature and phase transition temperature for d) organic and e) inorganic compounds with respect to Bi-doping concentration (obtained from TGA and DSC measurements).

© 2024 The Author(s). Small published by Wiley-VCH GmbH

16136829, 2024, 51, Downloaded from https://onlinelibrary.wiley.com/doi/10.1002/smll.202407141 by Ewha Womans University Library, Wiley Online Library on [16/01/2025]. See the Terms and Conditions (https://onlinelibrary.wiley.com/terms-and-conditions) on Wiley Online Library for rules of use; OA articles are governed by the applicable Creative Commons License

defect state and degrades the perovskite-based optoelectronic device performance[45] and as a result, several studies have attempted to eliminate these Pb^0 defects.

Tang et al. reported the absence of Pb^0 in Bi-doped $MAPbBr_3$ single crystals, attributing this to improved perovskite stability.[10] While our current study shows similar results, it remains difficult to claim that Pb^0 disappearance is proof of improved stability. XPS measurement is surface limited (≈ 5–10 nm below the surface), and hence strongly surface sensitive which means that the results may not fully represent the bulk material stability. This aspect will be addressed in the subsequent section.

We propose a possible hypothesis to explain the disappearance of Pb^0 and the presence of Bi^0: reduction potential (E°). Tang et al. suggested that Bi^{3+} is more easily transformed to Bi^0 (positive reduction potential, 0.31 V) than Pb^{2+} (negative reduction potential, -0.13 V).[46] Consequently, Bi^{3+} is more readily reduced to Bi^0 than Pb^{2+} to Pb^0. This hypothesis implies that Bi-doped perovskite might form Bi^0 when exposed to an X-ray beam rather than Pb^0. All our samples were subjected to identical measurement conditions, meaning that the presence of Bi^0 among the doped single crystals indicates that Bi does somehow reduce the formation of Pb^0. Further investigation is needed to elucidate the origin of Bi^0 and its impact on material stability.

2.3.2. Thermal Stability

The discussion above raised the possibility of an optimum doping concentration that limits stable Bi doping and a possibility of improving stability. We explored the thermal stability of the single crystals with TGA and DSC. Figure S11 (Supporting Information) shows TGA and differential thermogravimetry (DTG) graphs for undoped and doped samples to compare the mass loss behavior which will provide a better understanding of how Bi doping affects $MAPbBr_3$ decomposition. TGA curves confirm that all samples exhibit two weight loss steps. Step 1 indicates ≈24% weight loss due to the organic cation, and step 2 indicates ≈75% weight loss due to $PbBr_2$ degradation and evaporation, which has been previously observed for methylammonium lead trihalide perovskites.[47] The onset temperatures of the first step mass loss = 335.2 °C, 328.2 °C, 330.2 °C, 334.7 °C, 339.9 °C, and 339.9 °C for 0%, 0.019%, 0.042%, 0.063%, 0.11%, and 0.19% doped samples, respectively. The increasing Bi concentration in doped single crystals leads to higher thermal stability. We assume this is due to stronger chemical bonding observed through XPS. However, the low doping concentrations demonstrate a lower stability compared to the undoped single crystal which is expected to be a result of unstable incorporation of Bi in the crystal structure.

The second mass loss must also be considered to fully understand Bi doping effects on thermal stability as Bi substituting Pb is confirmed. Onset temperatures for step 2 of mass loss = 594.9 °C, 571.9 °C, 591.0 °C, 592.2 °C, 571.4 °C, and 534.5 °C for the 0%, 0.019%, 0.042%, 0.063%, 0.11%, and 0.19% doped samples, respectively. The 0.063% doped sample exhibits the highest stability for the inorganic compound among the doped samples supporting a threshold doping concentration that was suggested previously.

Figure S12 (Supporting Information) show DSC results used to monitor phase transition and support thermal stability effects. All cases exhibit two endothermic peaks, indicating phase transition from solid to gas for the organic and inorganic components,[47a] corresponding to the TGA curves. While the first endothermic peaks appear to have sharp and similar shapes among the samples, the second peaks exhibit significant shape differences after doping, which is expected to be altered by Bi incorporation. Sharp peaks are only sighted for the 0% and 0.063% samples, whereas 0.019%, 0.042%, 0.11%, and 0.19% samples exhibit a broad double peak which indicates impure samples. This probably indicates that an optimum doping concentration exists at 0.063%. Figure 6d,e summarizes the TGA and DSC temperatures which represent that the transition and decomposition temperatures for all the samples follow similar trends. The doping concentration of = 0.063% achieved is the most stabilized condition for the Bi substituting Pb site and hence exhibits the highest thermal stability among the doped samples.

3. Conclusion

This study investigated the effects of Bi doping on $MAPbBr_3$ single crystals to enhance the understanding of how various Bi concentrations influence the physical, and chemical properties, and stability of lead halide perovskites. XRD and low-frequency Raman spectroscopy confirmed that Bi incorporation compressed the crystal structure by substituting Pb at the B-site, leading to lattice contraction. The trends observed in optical and electrical properties suggest an optimal doping concentration ≈0.063%, where the doped single crystals exhibit the best characteristics.

A trade-off was observed between the induced defect states and enhancements in electrical conductivity, mobility, and carrier concentration, underscoring the importance of selecting the appropriate doping concentration for specific device applications. N-doping after Bi incorporation was revealed, and we exhibited organic bonding shortening, leading to stronger chemical bonding. This is attributed to increased organic decomposition temperature. Interestingly, the inorganic compound decomposition temperature exhibited a peak point at 0.063% among the doped samples, which supports our claim on the existence of an optimum doping concentration at 0.063%.

In conclusion, our work identified an optimal Bi doping condition at 0.063%, which overall possesses the best properties among the doped samples. The findings emphasize the importance of controlling doping concentration to achieve improved material properties, which can significantly benefit in widening and improving the performance of perovskite optoelectronic applications.

4. Experimental Section

Single Crystal Growth: All chemicals were used as received. The perovskite precursor solution was mixed from 1 M of $PbBr_2$ (99.99%, trace metals basis, Tokyo Chemistry Industry Co., Ltd), and CH_3NH_3Br (Greatcell Solar) in N, N-dimethylformamide (DMF, Sigma–Aldrich). For doped single crystals, $BiBr_3$ (Sigma–Aldrich) was added into the solution at various concentrations calculated relative to the molar ratio with $PbBr_2$. The final precursor solutions were mixed for 5 h to dissolve all components. The fully dissolved solutions were filtered with a 0.2 µm polytetrafluoroethylene filter. After filtration, the solution was heated on a hot plate at a slowly and regularly increasing temperature. Finally, the grown crystals were dried in a vacuum oven.

© 2024 The Author(s). Small published by Wiley-VCH GmbH

16136829, 2024, 51, Downloaded from https://onlinelibrary.wiley.com/doi/10.1002/smll.202407141 by Ewha Womans University Library, Wiley Online Library on [16/01/2025]. See the Terms and Conditions (https://onlinelibrary.wiley.com/terms-and-conditions) on Wiley Online Library for rules of use; OA articles are governed by the applicable Creative Commons License

Device Fabrication: Au electrodes (≈100 nm) were deposited by thermal evaporation on both sides of the single crystal in a high vacuum to fabricate the hole-only devices for SCLC measurement. For Hall effect measurement, the single crystals were covered with polyimide tape, except for the four edges where the Au electrodes were deposited by thermal evaporation.

Characterization: SEM and EDS analyses were used to analyze the surface and element distribution of the perovskite single crystals using field-emission scanning electron microscopy (FE-SEM, HITACHI SU8220) at the Western Seoul Center, Korea Basic Science Institute. XRD of the single crystals was performed on a Multipurpose XRD at the Western Seoul Center, Korea Basic Science Institute. Single crystal crushed powders were scanned on a D8 Advance.2020 multi-purpose XRD (Brucker) at the Research Institute of Advanced Materials (RIAM), Seoul National University. ICP-OES (Agilent, 5110) was used to investigate Bi and Pb quantities in the single crystals. The optical absorbance of the single crystals was measured through UV/Vis/NIR spectroscopy (Lambda 750). Raman spectroscopy was measured with a 633 nm laser (LabRAM HR Evolution) at the RIAM, Seoul National University. Steady–state PL measurements were performed on a FlouTime 300 with an excitation wavelength of 405 nm at the RIAM, Seoul National University. XPS and UPS were measured with a Thermo Scientific Nexsa G2 X-Ray Photoelectron Spectrometer (XPS) System at the Korea Institute of Science and Technology (KIST) Advanced Analysis Center. Current–voltage measurements were taken using a probe station with a Keithley 4200 semiconductor measurement system at room temperature. Hall effect measurement was performed on an Accent HL5500PC Hall Effect Measurement System at the Holonyak Micro & Nanotechnology Lab, University of Illinois Urbana-Champaign. Thermal stability was evaluated with TGA-DSC (STA 449 F1 Jupiter, NETZSCH) from 30 to 800 °C with a temperature ramping rate of 10K/min in an N_2 gas flow of 50 mL min^{-1}.

Supporting Information

Supporting Information is available from the Wiley Online Library or from the author.

Acknowledgements

This work was supported by the Basic Science Research Program through the National Research Foundation of Korea (NRF), funded by the Ministry of Education (NRF-2018R1A6A1A03025340) and a grant (NRF-2022M3J1A1064229) from the Technology Development Program for solving climate change through the National Research Foundation (NRF) funded by the Ministry of Science and ICT. The authors thank Professor Kyekyoon (Kevin) Kim and Frank Kelly for assistance with the Hall effect measurement at the University of Illinois Urbana-Champaign. This manuscript was written with the contributions of all authors. All authors have approved the final version of the manuscript.

Conflict of Interest

The authors declare no conflict of interest.

Data Availability Statement

Research data are not shared.

Keywords

bismuth, doping, lead halide perovskite, single crystal, stability

Received: August 15, 2024
Revised: September 17, 2024
Published online: October 9, 2024

[1] C. Quarti, G. Grancini, E. Mosconi, P. Bruno, J. M. Ball, M. M. Lee, H. J. Snaith, A. Petrozza, F. De Angelis, *J. Phys. Chem. Lett.* **2014**, *5*, 279.
[2] a) D. Shi, V. Adinolfi, R. Comin, M. Yuan, E. Alarousu, A. Buin, Y. Chen, S. Hoogland, A. Rothenberger, K. Katsiev, Y. Losovyj, X. Zhang, P. A. Dowben, O. F. Mohammed, E. H. Sargent, O. M. Bakr, *Science* **2015**, *347*, 519; b) L. Chen, Y.-Y. Tan, Z.-X. Chen, T. Wang, S. Hu, Z.-A. Nan, L.-Q. Xie, Y. Hui, J.-X. Huang, C. Zhan, S.-H. Wang, J.-Z. Zhou, J.-W. Yan, B.-W. Mao, Z.-Q. Tian, *J. Am. Chem. Soc.* **2019**, *141*, 1665; c) Q. Dong, Y. Fang, Y. Shao, P. Mulligan, J. Qiu, L. Cao, J. Huang, *Science* **2015**, *347*, 967; d) Z. Lian, Q. Yan, T. Gao, J. Ding, Q. Lv, C. Ning, Q. Li, J.-L. Sun, *J. Am. Chem. Soc.* **2016**, *138*, 9409; e) Z. Zhang, W. Kim, M. J. Ko, Y. Li, *Nano Converg.* **2023**, *10*, 23.
[3] a) T. Cai, J. Wang, W. Li, K. Hills-Kimball, H. Yang, Y. Nagaoka, Y. Yuan, R. Zia, O. Chen, *Adv. Sci.* **2020**, *7*, 2001317; b) Q. Wei, J. Yin, O. M. Bakr, Z. Wang, C. Wang, O. F. Mohammed, M. Li, G. Xing, *Angew. Chem., Int. Ed.* **2021**, *60*, 10957; c) C. Park, S. J. Yang, J. Choi, S. Song, W. Choi, K. Cho, *ChemSusChem* **2020**, *13*, 3261; d) A. L. Abdelhady, M. I. Saidaminov, B. Murali, V. Adinolfi, O. Voznyy, K. Katsiev, E. Alarousu, R. Comin, I. Dursun, L. Sinatra, E. H. Sargent, O. F. Mohammed, O. M. Bakr, *J. Phys. Chem. Lett.* **2016**, *7*, 295; e) X. Miao, T. Qiu, S. Zhang, H. Ma, Y. Hu, F. Bai, Z. Wu, *J. Mater. Chem. C* **2017**, *5*, 4931; f) M. Liu, G. Zhong, Y. Yin, J. Miao, K. Li, C. Wang, X. Xu, C. Shen, H. Meng, *Adv. Sci.* **2017**, *4*, 1700335; g) C. Zhang, A. Baktash, J. A. Steele, D. He, S. Ding, S. Penukula, M. Hao, R. Lin, J. Hou, N. Rolston, M. Lyu, P. Chen, W.-Q. Wu, L. Wang, *Adv. Funct. Mater.* **2024**, *34*, 2315897.
[4] a) Y. Hu, F. Bai, X. Liu, Q. Ji, X. Miao, T. Qiu, S. Zhang, *ACS Energy Lett.* **2017**, *2*, 2219; b) S. Kundu, D. Zhang, A. M. Askar, E. G. Moloney, M. M. Adachi, A. Nadeem, S. Moradi, V. Yeddu, A. L. Abdelhady, O. Voznyy, M. I. Saidaminov, *ACS Mater. Lett.* **2022**, *4*, 707.
[5] a) Y. Yamada, M. Hoyano, R. Akashi, K. Oto, Y. Kanemitsu, *J. Phys. Chem. Lett.* **2017**, *8*, 5798; b) P. K. Nayak, M. Sendner, B. Wenger, Z. Wang, K. Sharma, A. J. Ramadan, R. Lovrinčić, A. Pucci, P. K. Madhu, H. J. Snaith, *J. Am. Chem. Soc.* **2018**, *140*, 574; c) R. Meng, G. Wu, J. Zhou, H. Zhou, H. Fang, M. A. Loi, Y. Zhang, *Chem. - Eur. J.* **2019**, *25*, 5480; d) L. Han, L. Wu, C. Liu, J. Zhang, *J. Phys. Chem. C* **2019**, *123*, 8578; e) A. M. Ulatowski, A. D. Wright, B. Wenger, L. R. V. Buizza, S. G. Motti, H. J. Eggimann, K. J. Savill, J. Borchert, H. J. Snaith, M. B. Johnston, L. M. Herz, *J. Phys. Chem. Lett.* **2020**, *11*, 3681.
[6] M. Yavari, F. Ebadi, S. Meloni, Z. S. Wang, T. C.-J. Yang, S. Sun, H. Schwartz, Z. Wang, B. Niesen, J. Durantini, P. Rieder, K. Tvingstedt, T. Buonassisi, W. C. H. Choy, A. Filippetti, T. Dittrich, S. Olthof, J.-P. Correa-Baena, W. Tress, *J. Mater. Chem. A* **2019**, *7*, 23838.
[7] a) F.-X. Liang, J.-J. Jiang, Y.-Z. Zhao, Z.-X. Zhang, D. Wu, L.-H. Zeng, Y. H. Tsang, L.-B. Luo, *Adv. Funct. Mater.* **2020**, *30*, 2001033; b) X. Wang, Y. Xu, Y. Pan, Y. Li, J. Xu, J. Chen, J. Wu, Q. Li, X. Zhang, Z. Zhao, C. Li, E. E. Elemike, D. C. Onwudiwe, J. Akram, W. Lei, *Nano Energy* **2021**, *89*, 106311; c) Y. Pan, X. Wang, Y. Liao, Y. Xu, Y. Li, Q. Li, X. Zhang, J. Chen, Z. Zhu, Z. Zhao, E. E. Elemike, M. Furuta, W. Lei, *ACS Appl. Mater. Interfaces* **2022**, *14*, 50331; d) V. Anilkumar, A. Mahapatra, J. Nawrocki, R. D. Chavan, P. Yadav, D. Prochowicz, *Adv. Opt. Mater.* **2023**, *12*, 2302032.
[8] Y. Jin, D. H. Keum, S.-J. An, J. Kim, H. S. Lee, Y. H. Lee, *Adv. Mater.* **2015**, *27*, 5534.
[9] Y. Cho, H. R. Jung, Y. S. Kim, Y. Kim, J. Park, S. Yoon, Y. Lee, M. Cheon, S. Y. Jeong, W. Jo, *Nanoscale* **2021**, *13*, 8275.
[10] W. Tang, J. Zhang, S. Ratnasingham, F. Liscio, K. Chen, T. Liu, K. Wan, E. S. Galindez, E. Bilotti, M. Reece, M. Baxendale, S. Milita, M. A. McLachlan, L. Su, O. Fenwick, *J. Mater. Chem. A* **2020**, *8*, 13594.
[11] E. Jedlicka, J. Wang, J. Mutch, Y.-K. Jung, P. Went, J. Mohammed, M. Ziffer, R. Giridharagopal, A. Walsh, J.-H. Chu, D. S. Ginger, *J. Phys. Chem. Lett.* **2021**, *12*, 2749.
[12] V. M. Goldschmidt, *Sci. Nat.* **1926**, *14*, 477.

© 2024 The Author(s). Small published by Wiley-VCH GmbH

16136829, 2024, 51, Downloaded from https://onlinelibrary.wiley.com/doi/10.1002/smll.202407141 by Ewha Womans University Library, Wiley Online Library on [16/01/2025]. See the Terms and Conditions (https://onlinelibrary.wiley.com/terms-and-conditions) on Wiley Online Library for rules of use; OA articles are governed by the applicable Creative Commons License

[13] a) H. Rietveld, *J. Appl. Crystallogr.* **1969**, *2*, 65; b) J. Rodríguez-Carvajal, *Phys. B: Condens. Matter* **1993**, *192*, 55.
[14] R. Shannon, *Acta Cryst. A* **1976**, *32*, 751.
[15] a) H. R. Jung, G. Y. Kim, B. P. Nguyen, H.-J. Jin, W. Jo, T. T. Thu Nguyen, S. Yoon, W. S. Woo, C. W. Ahn, S. Cho, I. W. Kim, *J. Phys. Chem. C* **2017**, *121*, 21930; b) L. C. Schmidt, A. Pertegás, S. González-Carrero, O. Malinkiewicz, S. Agouram, G. Mínguez Espallargas, H. J. Bolink, R. E. Galian, J. Pérez-Prieto, *J. Am. Chem. Soc.* **2014**, *136*, 850.
[16] a) R. G. Niemann, A. G. Kontos, D. Palles, E. I. Kamitsos, A. Kaltzoglou, F. Brivio, P. Falaras, P. J. Cameron, *J. Phys. Chem. C* **2016**, *120*, 2509; b) M. Li, K. Bu, J. Li, H. Wang, Y. Xu, S. Guo, H. Luo, B. Liu, D. Yang, Y. Gong, Y. Wang, Y. Liu, X. Lü, C. Lin, *Chem. Mater.* **2023**, *35*, 1177.
[17] L. Q. Xie, T. Y. Zhang, L. Chen, N. Guo, Y. Wang, G. K. Liu, J. R. Wang, J. Z. Zhou, J. W. Yan, Y. X. Zhao, B. W. Mao, Z. Q. Tian, *Phys. Chem. Chem. Phys.* **2016**, *18*, 18112.
[18] M. R. Joya, K. M. Fonseca, J. Barba-Ortega, *AIP Conf. Proc* **2014**, *1627*, 42.
[19] Y. Yang, J. P. Robbins, L. Ezeonu, Y. Ma, N. Sparta, X. Kong, S. Strauf, S. G. Podkolzin, S. S. Lee, *J. Mater. Chem. C* **2020**, *8*, 8896.
[20] Y. Chen, Y. Lei, Y. Li, Y. Yu, J. Cai, M.-H. Chiu, R. Rao, Y. Gu, C. Wang, W. Choi, H. Hu, C. Wang, Y. Li, J. Song, J. Zhang, B. Qi, M. Lin, Z. Zhang, A. E. Islam, B. Maruyama, S. Dayeh, L.-J. Li, K. Yang, Y.-H. Lo, S. Xu, *Nature* **2020**, *577*, 209.
[21] W. Bi, N. Leblanc, N. Mercier, P. Auban-Senzier, C. Pasquier, *Chem. Mater.* **2009**, *21*, 4099.
[22] Y. Rakita, S. R. Cohen, N. K. Kedem, G. Hodes, D. Cahen, *MRS Commun.* **2015**, *5*, 623.
[23] L. Han, W. Long, J. Zhang, L. Wu, C. Liu, *J. Cryst. Growth* **2020**, *537*, 125604.
[24] a) G. Batignani, G. Fumero, A. R. Srimath Kandada, G. Cerullo, M. Gandini, C. Ferrante, A. Petrozza, T. Scopigno, *Nat. Commun.* **2018**, *9*, 1971. b) B. Dhanabalan, Y.-C. Leng, G. Biffi, M.-L. Lin, P.-H. Tan, I. Infante, L. Manna, M. P. Arciniegas, R. Krahne, *ACS Nano* **2020**, *14*, 4689; c) W. Zhao, Z. Qin, C. Zhang, G. Wang, X. Dai, M. Xiao, *Appl. Phys. Lett.* **2019**, *115*, 243101.
[25] a) F. Capitani, C. Marini, S. Caramazza, P. Dore, A. Pisanu, L. Malavasi, L. Nataf, F. Baudelet, J. B. Brubach, P. Roy, P. Postorino, *J. Phys. Chem. C* **2017**, *121*, 28125; b) F. H. Naqvi, J.-H. Ko, T. H. Kim, C. W. Ahn, Y. Hwang, M. Sheraz, S. Kim, *J. Korean Phys. Soc.* **2022**, *81*, 230.
[26] K.-H. Wang, L.-C. Li, M. Shellaiah, K. W. Sun, *Sci. Rep.* **2017**, *7*, 13643.
[27] A. M. A. Leguy, A. R. Goñi, J. M. Frost, J. Skelton, F. Brivio, X. Rodríguez-Martínez, O. J. Weber, A. Pallipurath, M. I. Alonso, M. Campoy-Quiles, M. T. Weller, J. Nelson, A. Walsh, P. R. F. Barnes, *Phys. Chem. Chem. Phys.* **2016**, *18*, 27051.
[28] B. Wenger, P. K. Nayak, X. Wen, S. V. Kesava, N. K. Noel, H. J. Snaith, *Nat. Commun.* **2017**, *8*, 590.
[29] F. Lyu, X. Zheng, Y. Wang, R. Shi, J. Yang, Z. Li, J. Yu, B.-L. Lin, *J. Mater. Chem. A* **2019**, *7*, 15627.
[30] B. Subedi, C. Li, C. Chen, D. Liu, M. M. Junda, Z. Song, Y. Yan, N. J. Podraza, *ACS Appl. Mater. Interfaces* **2022**, *14*, 7796.
[31] J. Zhu, L. Zhou, Y. Zhu, J. Huang, L. Hou, J. Shen, S. Dai, C. Li, *Small* **2022**, *18*, 2104399.
[32] L. Bian, F. Cao, L. Li, *Small* **2023**, *19*, 2302700.
[33] a) Y. Fang, H. Wei, Q. Dong, J. Huang, *Nat. Commun.* **2017**, *8*, 14417; b) T. Yamada, Y. Yamada, Y. Kanemitsu, *J. Lumin.* **2020**, *220*, 116987.
[34] Y.-H. Kim, C. Wolf, Y.-T. Kim, H. Cho, W. Kwon, S. Do, A. Sadhanala, C. G. Park, S.-W. Rhee, S. H. Im, R. H. Friend, T.-W. Lee, *ACS Nano* **2017**, *11*, 6586.
[35] a) M. Luo, S. Yan, C. Wei, L. Xue, C. Liu, O. E. Fayemi, B. S. Bae, S. B. Shafie, M. Xiao, Q. Li, Z. Zhao, J. Wu, W. Lei, X. Zhang, *Adv. Mater. Interfaces* **2022**, *9*, 2200450; b) C. Wei, W. Su, J. Li, B. Xu, Q. Shan, Y. Wu, F. Zhang, M. Luo, H. Xiang, Z. Cui, H. Zeng, *Adv. Mater.* **2022**, *34*, 2107798.
[36] S. S. Youn, J. Kim, J. Na, W. Jo, G. Y. Kim, *ACS Appl. Mater. Interfaces* **2022**, *14*, 48229.
[37] J. Kim, J. Park, Y.-H. Kim, W. Jo, *Small* **2022**, *18*, 2204173.
[38] G. Shao, *Energy Environ. Mater.* **2021**, *4*, 273.
[39] Z. Hawash, S. R. Raga, D.-Y. Son, L. K. Ono, N.-G. Park, Y. Qi, *J. Phys. Chem. Lett.* **2017**, *8*, 3947.
[40] N. Phung, R. Félix, D. Meggiolaro, A. Al-Ashouri, G. Sousa e Silva, C. Hartmann, J. Hidalgo, H. Köbler, E. Mosconi, B. Lai, R. Gunder, M. Li, K.-L. Wang, Z.-K. Wang, K. Nie, E. Handick, R. G. Wilks, J. A. Marquez, B. Rech, T. Unold, J.-P. Correa-Baena, S. Albrecht, F. De Angelis, M. Bär, A. Abate, *J. Am. Chem. Soc.* **2020**, *142*, 2364.
[41] A. Y. Teterin, Y. A. Teterin, K. I. Maslakov, V. G. Yarzhemskiĭ, S. E. Sverchkov, B. I. Denker, B. I. Galagan, L. D. Iskhakova, L. I. Bulatov, V. V. Dvoĭrin, V. M. Mashinskiĭ, A. A. Umnikov, A. N. Gur'yanov, V. I. Nefedov, E. M. Dianov, *Dokl. Phys.* **2008**, *53*, 566.
[42] J. Liang, X. Hu, C. Wang, C. Liang, C. Chen, M. Xiao, J. Li, C. Tao, G. Xing, R. Yu, W. Ke, G. Fang, *Joule* **2022**, *6*, 816.
[43] G. Armaroli, L. Ferlauto, F. Lédée, M. Lini, A. Ciavatti, A. Kovtun, F. Borgatti, G. Calabrese, S. Milita, B. Fraboni, D. Cavalcoli, *ACS Appl. Mater. Interfaces* **2021**, *13*, 58301.
[44] J. D. McGettrick, K. Hooper, A. Pockett, J. Baker, J. Troughton, M. Carnie, T. Watson, *Mater. Lett.* **2019**, *251*, 98.
[45] L. Wang, H. Zhou, J. Hu, B. Huang, M. Sun, B. Dong, G. Zheng, Y. Huang, Y. Chen, L. Li, Z. Xu, N. Li, Z. Liu, Q. Chen, L.-D. Sun, C.-H. Yan, *Science* **2019**, *363*, 265.
[46] W. Tang, T. Liu, M. Zhang, F. Yuan, K. Zhou, R. Lai, Y. Lian, S. Xing, W. Xiong, M. Zhang, F. Gao, B. Zhao, D. Di, *Matter* **2023**, *6*, 3782.
[47] a) A. Dualeh, P. Gao, S. I. Seok, M. K. Nazeeruddin, M. Grätzel, *Chem. Mater.* **2014**, *26*, 6160; b) M. Nazim, A. A. Parwaz Khan, F. Khan, S. K. Cho, R. Ahmad, *Nanoscale Adv.* **2022**, *4*, 2729.

© 2024 The Author(s). Small published by Wiley-VCH GmbH

16136829, 2024, 51, Downloaded from https://onlinelibrary.wiley.com/doi/10.1002/smll.202407141 by Ewha Womans University Library, Wiley Online Library on [16/01/2025]. See the Terms and Conditions (https://onlinelibrary.wiley.com/terms-and-conditions) on Wiley Online Library for rules of use; OA articles are governed by the applicable Creative Commons License